Radiometric Calibration by Rank Minimization

Joon-Young Lee, *Student Member, IEEE,* Yasuyuki Matsushita, *Senior Member, IEEE,* Boxin Shi, In So Kweon, *Member, IEEE,* and Katsushi Ikeuchi, *Fellow, IEEE*

Abstract—We present a robust radiometric calibration framework that capitalizes on the transform invariant low-rank structure in the various types of observations, such as sensor irradiances recorded from a static scene with different exposure times, or linear structure of irradiance color mixtures around edges. We show that various radiometric calibration problems can be treated in a principled framework that uses a rank minimization approach. This framework provides a principled way of solving radiometric calibration problems in various settings. The proposed approach is evaluated using both simulation and real-world datasets and shows superior performance to previous approaches.

Index Terms—radiometric calibration, camera response function, rank minimization, low-rank structure

1 Introduction

The radiometric response function relates sensor irradiance and image brightness values. In most cameras, there exists a non-linear radiometric response function for purposes such as compressing the dynamic range of sensor irradiance or adapting to a display's non-linear mappings. The non-linearity is intentionally designed by camera manufacturers for enhancing the visual quality of recorded images. However, for computer vision applications, this non-linearity causes problems, especially when a linear relationship between the sensor irradiance and the recorded intensity is explicitly assumed. For example, photometric approaches like shape-from-shading and photometric stereo methods generally assume a linear (or affine) mapping from the physical scene brightness to the image intensity. If the non-linear mapping is not accounted for in such methods, it leads to unexpected error in the computed results. Therefore, radiometric calibration is an important first step for various computer vision algorithms that assume a linear mapping to make them work correctly.

The problem of radiometric calibration is determining the non-linear camera response function from observations. The observations can be multiple images taken with different exposure times from a fixed camera location [1], [2], color distributions around image edges [3], or color profiles obtained from varying lightings [4]. In all of these cases, recovering radiometric response functions without additional knowledge or assumptions is an under-constrained problem. Since these methods use different observations, they naturally use different assumptions and criteria for recovering the response functions. Our key observation is that a class of radiometric calibration methods rely on a certain *linearity* defined in spaces that they use.

Based on this observation, we formulate the radiometric calibration problem in a unified and principled framework. Our method capitalizes on the fundamental linear dependency of sensor irradiances. Our method arranges the observations (*e.g.*, multiple images obtained with different exposure times, or multiple images with varying illumination, and etc.) in a matrix form, where a column vector corresponds to an observation vector. When the linear relationship is observed in such a matrix, the rank of the matrix ideally becomes one. On the other hand, when the response function is non-linear, the matrix generally becomes higher or even full rank. From this observation, we develop a framework for radiometric calibration problems using a matrix rank minimization technique (see Fig. 1).

There are a few benefits from casting the problem in this manner. First of all, the rank minimization approach can efficiently avoid the over-fitting problem. While there exist robust approaches [5] that are not affected by the over-fitting problem, still the problem is commonly observed in previous approaches [2] that rely on the ℓ^2-norm minimization. Second, it gives a unified framework for solving the radiometric calibration problem by explicitly using the linear dependency of the irradiance vectors. With this framework, various radiometric calibration problems can be treated in the same manner, and therefore gives a better understanding to the problem. Third, because of the new formulation, we can utilize an advanced rank minimization technique that can reliably derive the solution in a principled manner.

In presenting our work, we begin by briefly describing the radiometric response function and reviewing related works.

- *J.-Y. Lee and I. S. Kweon are with the Department of Electrical Engineering, KAIST, Korea.*
  E-mail: jylee@rcv.kaist.ac.kr, iskweon@ee.kaist.ac.kr
- *Y. Matsushita is with Microsoft Research Asia, Beijing, China.*
  Email: yasumat@microsoft.com
- *B. Shi and K. Ikeuchi are with Institute of Industrial Science, the University of Tokyo, Japan.*
  Email: {shi, ki}@cvl.iis.u-tokyo.ac.jp

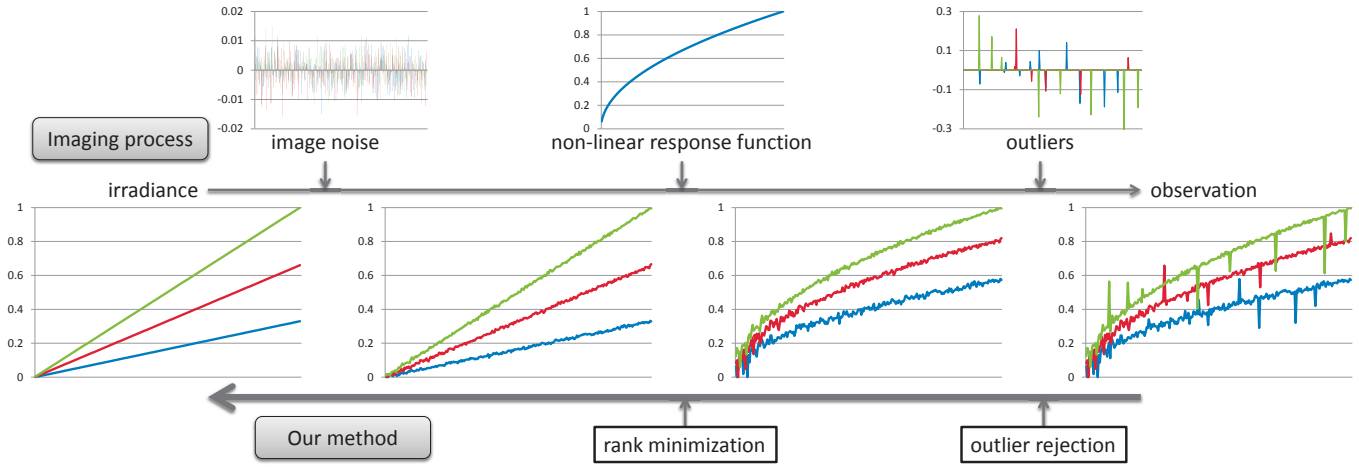

Fig. 1. Illustration of our approach. Our method arranges the observations (*e.g.*, multiple images obtained with different exposure times, or color profiles obtained from image edges, etc.) in a matrix form, where a column vector corresponds to an observation vector. In the matrix form, the irradiance matrix should be rank-1, while the observations matrix generally has a higher rank. Our method seeks the inverse response function that transforms the observation matrix into a low-rank matrix.

1.1 Radiometric response function

The radiometric response function relates the sensor irradiance I and recorded intensity value M (observation) by

$$M = f(I). \tag{1}$$

In the case of color cameras, color channel has an independent mapping. With assumptions of monotonicity and continuity, the response function $f : \mathbb{R} \rightarrow \mathbb{R}$ can be uniquely inverted to an inverse response function $g = f^{-1}$ if we neglect quantization and clipping error. Using the inverse response function g, the recorded intensity values can be linearized by $g(M)$. Since what is available as input are the observations M, most radiometric calibration methods aim at recovering the inverse response function g. Once we know the inverse response function g, we can automatically determine the response function f with the aforementioned assumptions.

1.2 Prior work

There are various approaches for radiometric calibration. One widely-used approach takes as input a set of images recorded with varying exposures from a fixed camera. The early work by Mann and Picard [6] and Debevec and Malik [1] show that the response function can be recovered using images acquired by a static camera but with known exposure ratios. Mann and Picard [6] use a gamma correcting function to represent response functions. Debevec and Malik [1] assume a smoothness property of response functions and estimate them in a non-parametric manner. Mitsunaga and Nayar's method [2] uses a parametric yet flexible representation, *i.e.*, a polynomial representation. Using approximate prior knowledge of the ratios of exposures, their approach iteratively estimates response functions and accurate ratios of the exposures. Grossberg and Nayar [7] create a database of real-world camera response functions (DoRF) and use it for better representation of response functions. Instead of taking a set of images, Nayar and Mitsunaga [8] use an optical mask to capture an image with spatially varying pixel exposures.

There are a few prior approaches that allow some camera movement or scene motion. In Mann and Mann's method [9], images are taken by a rotating and zooming camera and the method simultaneously estimates the response function with a non-parametric model, as well as the exposure ratios. Grossberg and Nayar [10] use intensity histograms of two images of different exposures instead of finding exact pixel correspondence for determining response functions from image sequences with camera/scene movement. Litvinov and Schechner [11] propose an approach for simultaneously estimating the radiometric response, spatial non-uniformity, and gain variations from an image sequence acquired during camera motion. Kim and Pollefeys's method [5] allows for free movement of the camera and some motion in the scene by dynamic programming on the joint histogram built from correspondences. As pointed out in [5], [10], [11], without the knowledge of exposure ratios, the estimate still has an *exponential ambiguity*. While not unique, such an estimate is still useful for many applications, such as radiometric alignment, high dynamic range (HDR) image production, and smooth image stitching.

Instead of using varying exposures, some approaches use statistical properties embedded in images to achieve radiometric calibration. Farid [12] presents a blind gamma estimation by minimizing specific higher-order correlations in the frequency domain. Tsin *et al.*'s

method [13] estimates non-parametric response functions using a statistical model of the CCD imaging process. Pal *et al*. [14] use probabilistic imaging models and weak prior models for deriving response functions to produce high-quality HDR images. Ng *et al*. [15] present a geometry invariance-based method with a generalized gamma curve representation for estimating response functions. Matsushita and Lin [16] propose to use the symmetric property of image noise by observing noise distributions contained in images. Takamatsu *et al*. [17] improve the noise-based method with a probabilistic intensity similarity measure, which requires a fewer number of images. In [18], Takamatsu *et al*. derive the relationship between the response function and noise variances, and estimate response functions using the image noise variance. In a more general setting, Lin *et al*. [3] and Lin and Zhang [19] propose methods that take only a single image as input. Their methods use edges for obtaining color or gray-scale histogram distributions, and the optimal inverse response function is determined by transforming the observed non-linear distributions into linear distributions. A similar idea is introduced by Wilburn *et al*. [20]. Wilburn *et al*. [20] use temporal irradiance mixtures caused by motion blur, instead of spatial mixtures at edges.

There are some other methods which use varying illumination conditions [4], [21], [22], [23]. Manders *et al*. [21] use the superposition property of light, and Shafique and Shah [22] use illumination and geometric invariants. Kim *et al*. [23] present a method to use natural lighting conditions to obtain exposure changes. Shi *et al*. [4] perform calibration by linearizing a set of color values at the same coordinate from images taken under varying lighting conditions in a photometric stereo setting.

The idea of utilizing low-rank structures in real-world scenes has been used in various other vision problems. For example, the low-rank representation is shown to be useful for face recognition [24], structure from motion [25], and photometric stereo [26]. In more recent works, low-rank structure is widely explored in various novel applications with an emphasis on advanced optimization techniques. Peng *et al*. [27] align multiple images of objects of interest to a fixed canonical template to make the measurement on image similarity more accurate for recognition or classification purposes. These aligned images naturally bear the low-rank property. Paladini *et al*. [28] propose a variant shape model called a 3D-implicit low-rank shape model to represent the shape and apply it to non-rigid structure from motion. Zhang *et al*. [29] propose a transform invariant low-rank texture to deal with images containing camera projection deformations such as affine or projective transformations. Wu *et al*. [30] robustly solve photometric stereo in the presence of large and sparse errors such as specularity by extracting low-rank structure from the input matrix. Zhang *et al*. [31] present a method for estimating a camera's intrinsic and extrinsic parameters and lens distortion from low-rank textures that appear in images. All these current research works show the variety and validity of low-rank structures that exist in the real-world.

A preliminary version of this paper that focuses on radiometric calibration from multiple-exposure images appeared in [32]. We extend the work by defining a unified framework that treats a class of radiometric calibration problems in the same manner. With the proposed framework, we show that outliers can be efficiently handled with a simple optimization algorithm. Also, we perform extensive experiments with carefully redesigned simulations and in-depth analysis for analyzing the behavior of the proposed method.

2 Low-rank Structure in Calibrated Observations

Our method casts the radiometric calibration problem as a low-rank structure recovery problem. As described in the previous section, there are various approaches for radiometric calibration depending on the type of observations, *e.g*., a set of images with varying exposures, a set of images with varying illuminations, or a single image that contains irradiance mixtures around edges. We first show that these radiometric calibration problems that use the linearity in sensor irradiance can be formulated as a rank minimization problem.

Suppose we are given a set of observation vectors $\{\mathrm{vec}(M_1), \ldots, \mathrm{vec}(M_n)\}$ where each observation vector is defined as a vector of measured intensities $\mathrm{vec}(M_i) \in \mathbb{R}^{m\times 1}$. The numbers m and n represent the number of elements in each observation vector $\mathrm{vec}(M_i)$ and the number of observation vectors, respectively. We create an observation matrix $D \in \mathbb{R}^{m\times n}$ by stacking all the observation vectors $\mathrm{vec}(M_i)$ as

$$D = [\mathrm{vec}(M_1) \mid \cdots \mid \mathrm{vec}(M_n)]\,. \tag{2}$$

If we know the inverse response function $g(= f^{-1})$, the observation matrix D can be transformed into an irradiance matrix A with a scaling ambiguity by

$$g \circ D = A = [\mathrm{vec}(I_1) \mid \cdots \mid \mathrm{vec}(I_n)]\,, \tag{3}$$

where $\circ$ is an operator that describes the element-wise mapping, and $\mathrm{vec}(I_i) \in \mathbb{R}^{m\times 1}$ represents an irradiance vector. For the problems that we discuss, because the irradiance vectors $\mathrm{vec}(I_i)$ should be linearly dependent, the rank of the irradiance matrix A becomes one. Therefore, the problem of radiometric calibration can be formulated as determining the inverse response function g that minimizes the rank of the transformed matrix $g \circ D(= A)$:

$$\hat{g} = \underset{g}{\mathrm{argmin}}\, \mathrm{rank}\,(A) \quad \text{s.t.} \quad A = g \circ D. \tag{4}$$

This formulation is fairly general and capable of treating various types of observation vectors in a unified framework. The only requirement is to arrange the observation vectors in a way that they exhibit linear-dependency

after transformation by the correct inverse response function g. In the following, we describe the usage of this framework with different types of observation vectors.

2.1 Multiple-exposure case

One of the most widely used radiometric calibration methods uses multiple images of a static scene taken from a fixed camera with various exposures, such as Mitsunaga and Nayar's method [2]. In this setting, because the scene radiance L is constant, the sensor irradiance I becomes proportional to the exposure time e as

$$I = kLe \propto e, \tag{5}$$

with a constant scaling k. For each exposure, an observation vector $\mathrm{vec}(M_i)$ is created by vectorizing the image of m pixels, *e.g.*, by arranging recorded intensities in a scanline order. Given n different exposures, the observation matrix D can be created by stacking n observation vectors as Eq. (2). While we cannot directly observe the (vectorized) sensor irradiance $\mathrm{vec}(I_i)$, we know that the irradiance is proportional to the exposure time from Eq. (5). In other words, we know the irradiance matrix $A = [\mathrm{vec}(I_1) \mid \cdots \mid \mathrm{vec}(I_n)]$ becomes rank-1. Therefore, we can directly use the rank minimization formulation of Eq. (4) for the radiometric calibration problem in this setting, *i.e.*, finding the inverse response function g that best minimizes the rank of transformed observation matrix $g \circ D$.

2.2 Varying illumination case

Recently, Shi *et al*. [4] showed that radiometric calibration from photometric stereo images can be performed by linearizing the color profiles. The color profile is defined as an ordered set of color values in the RGB color space. Their method capitalizes on the property that color profiles form straight lines in the RGB color space if the response function is linear, while non-linear response functions f bend color profiles to be non-linear. Their method therefore seeks the inverse response function g that linearizes all the color profiles that are observed.

It is straightforward to cast their problem into our low-rank computation scheme. By treating each color profile as an observation matrix, we can cast the linearization problem as a matrix rank minimization problem. The color profile matrix should become rank-1 when the correct inverse response function is applied.

Given images captured under n different lighting conditions, we can form a color profile matrix $D \in \mathbb{R}^{3\times n}$ from each pixel location. The number of matrix rows corresponds to the number of color channels (RGB). For each of m pixels we have such a matrix $D_i,\ i = 1, \ldots, m$. If a correct inverse response function g is found, it transforms the observation matrix D_i to an irradiance matrix A_i, where the rank of A_i is one. Using all the pixels, we have an objective function written as:

$$\hat{g} = \underset{g}{\mathrm{argmin}} \sum_{i=1}^{m} \mathrm{rank}\,(A_i) \quad \text{s.t.} \quad A_i = g \circ D_i. \tag{6}$$

Notice that it computes a single global inverse response function g by minimizing the rank of all the color profile matrices. Thus, the radiometric calibration problem in this setting can be solved in the same computation manner as discussed in the previous section.

2.3 Color mixture case

There are radiometric calibration approaches that use color/irradiance mixtures in an observed image. Lin *et al*. use spatial color mixtures around edges [3], and Wilburn *et al*. use temporal irradiance mixtures of motion blur [20]. The color/irradiance mixtures are observed around image edges where two different radiances are mixed together due to the limited spatial resolution of the image array or temporal motion blur. In edge regions, RGB colors are linearly mixed together, however, observed intensities have non-linearity due to non-linear response functions. These methods use this property for estimating the inverse response function by transforming non-linear edge color distributions to linear ones.

Our method can also be applied to this setting in a similar manner with the previous varying-illumination setting. The difference is that a color mixture forms a line passing through two different color values in the RGB space, while a color profile always passes through the origin. To apply our rank-minimization approach, we translate the color mixture profile so as to pass through the origin by simply subtracting the RGB value of either color from the color mixture profile. This operation is to avoid offsets in the data; in this manner, we convert the affine problem into a linear problem. After the coordinate transform of the observation matrix, the exactly same formulation as Eq. (6) can be applied in this setting.

3 Calibration Algorithm

To efficiently compute the rank minimization problem, previous approaches use an approximate solution method that minimizes a nuclear norm [33], which is defined as the sum of the singular values $||A||_* \doteq \sum_{i=1}^{n} \sigma_i\,(A)$. The nuclear norm minimization turned out to be an effective computation tool that can be applied to problems when the transformation does not alter the magnitude of matrix elements.

In our case, however, nuclear norm minimization cannot be directly employed because the function g significantly alters the absolute values of matrix elements, and it therefore results in variations of the singular value magnitudes. When nuclear norm minimization is directly applied in this setting, the optimization prefers a degenerate solution where the inverse response function g tries to turn matrix elements into zero so that the singular values become smaller. To resolve this issue, we instead use condition numbers κ_i, *i.e.*, a ratio of singular values, defined as

$$\kappa_i(A) \doteq \sigma_i(A)/\sigma_1(A), \quad i = 2, 3, \ldots, n. \tag{7}$$

With the condition numbers κ_i, we can work with the relative magnitudes of the singular values that are unaffected by their absolute magnitudes. Now we approximate the energy functional (4) as a minimization of the summation of condition numbers as:

$$\hat{g} = \underset{g}{\operatorname{argmin}} \sum_{i=2}^{n} \kappa_i (A) \quad \text{s.t.} \quad A = g \circ D. \tag{8}$$

There are two main factors causing rank variations: non-linearity of response function and image noise. To see these effects, let us take synthetic response functions ($RF1 - 4$) shown in Fig. 2 as an example. The top half of Table 1 shows condition numbers $\kappa_2, \ldots, \kappa_5$ obtained from synthetic data that have five different exposure times for each response function. κ_{all} indicate the sum of condition numbers. Depending on the shape of the response function, condition numbers vary in the table. With the ideal linear response function $RF1$, all condition numbers become zero, which indicates rank-1 structure. With other more general non-linear response functions, however, the condition number κ_2 becomes significantly larger than other condition numbers. This is commonly observed because of the smooth (or low-frequency) characteristics of response functions.

In addition, the effect of noise also changes the condition numbers. To investigate of the effect of noise, we add image noise to the irradiance using a Poisson noise model [34]. In [34], the Poisson noise η_e is modeled as

$$\eta_e \doteq I_e - \mu \quad \text{s.t.} \quad I_e \sim f_P(I_e|\mu) = \frac{\mu^{(I_e)} e^{-\mu}}{(I_e)!}, \tag{9}$$

where I_e is a noisy observation that follows a Poisson distribution with a variance μ. The Poisson distribution is shifted by μ, therefore the mean of image noise η_e is zero. The variance μ is determined for each irradiance I as

$$\mu(I) = R_I I + D_I, \tag{10}$$

where R_I is a scalar parameter for signal-dependent shot noise, and D_I refers to dark current noise. We represent both parameters R_I and D_I as functions of the camera gain C_g and empirically determine them as

$$R_I = 0.035 C_g, \quad D_I = 0.1 C_g^2, \tag{11}$$

using images captured from a Point Grey Scorpion camera for this test. The response functions are applied after adding the noise with the camera gain $C_g = 3$ to the irradiances. These signals are quantized at 256 levels, and then the condition numbers are re-computed. The average condition numbers of 100 trials are shown in the bottom half of Table 1. The image noise makes the condition numbers similar across diverse response functions. It becomes more obvious in the higher condition numbers, *e.g.*, $\kappa_3 \ldots \kappa_5$, because the noise almost evenly affects all the condition numbers while the signals in the higher condition numbers have smaller values. In the absence of noise, we can achieve the same result from minimizing κ_{all} and minimizing κ_2. However, in the presence of noise, signal-to-noise ratios of the higher condition numbers rapidly degrade, therefore minimizing κ_{all} as Eq. (8) may cause an over-fitting result. For example, it shows that κ_{all} of $RF4$ is smaller than κ_{all} of $RF1$ in Table 1 with noise. From these observations, we use only the condition number κ_2 instead of using all the condition numbers. Therefore, the objective function is simplified from Eq. (8) to

$$\hat{g} = \underset{g}{\operatorname{argmin}} \kappa_2 (A) \quad \text{s.t.} \quad A = g \circ D. \tag{12}$$

This objective function is different from recent sparse and low-rank decompositions [27], [29], [30], which are based on the robust principal component analysis (PCA) algorithm [33]. The goal of sparse and low-rank decomposition is to find the minimum rank automatically in the presence of *sparse* outliers, while our objective function finds the best rank-1 matrix in the presence of noise that is not necessarily sparse. In other words, we explicitly use the prior knowledge about the rank-1 structure for efficiently solving the problem in this setting.

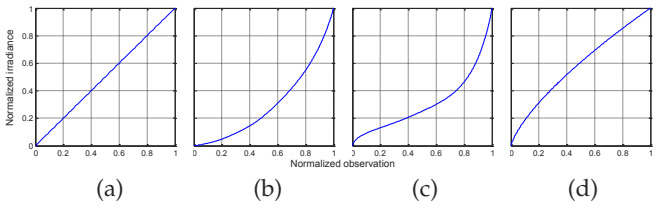

Fig. 2. Reference response functions used for Table 1. (a) Ideal linear response function ($RF1$). (b-d) Non-linear response functions ($RF2 - 4$).

condition number		κ_2	κ_3	κ_4	κ_5	κ_{all}
without noise	RF 1	0.0000	0.0000	0.0000	0.0000	0.0000
	RF 2	0.0284	0.0035	0.0009	0.0004	0.0332
	RF 3	0.1171	0.0186	0.0025	0.0000	0.1383
	RF 4	0.0028	0.0000	0.0000	0.0000	0.0028
with noise	RF 1	0.0178	0.0127	0.0097	0.0078	0.0480
	RF 2	0.0316	0.0157	0.0140	0.0123	0.0737
	RF 3	0.1181	0.0258	0.0150	0.0058	0.1646
	RF 4	0.0199	0.0107	0.0065	0.0044	0.0416

TABLE 1
Variations of condition numbers w.r.t. response functions illustrated in Fig. 2. Top half shows the condition numbers of the response functions $RF1 - 4$. Bottom half shows the case when noise is added.

3.1 Monotonicity constraint

In general, response functions as well as inverse response functions are monotonic functions. To avoid trivial solutions, we enforce this property during the computation by putting a monotonicity constraint, which is represented as $\partial g / \partial D > 0$. The constraint can be implemented as either hard or soft constraints. We empirically

employ a soft constraint because it can be well solved by a simple optimization method. With this constraint, the final form of the objective function becomes

$$\hat{g} = \underset{g}{\operatorname{argmin}}\, \kappa_2(A) + \lambda \sum_t H\left(-\frac{\partial g(t)}{\partial D}\right) \quad \text{s.t.} \quad A = g \circ D, \tag{13}$$

where $H(\cdot)$ is the Heaviside step function ($H(x) = 1$ when $x \geq 0$, and $H(x) = 0$, otherwise). The derivatives $\partial g(t)/\partial D$ are assessed by sampling $g(t)$ at various t in the range of $[0, 1]$.

3.2 Handling outliers

While we see that our method is robust against high frequency noise in the previous section, systematic outliers can still cause drifting during the optimization. In radiometric calibration, there exist various outliers due to misalignment of images, small motions in a scene, shadows, and so on. We develop a method based on robust PCA [33] for reliably rejecting these outliers. Robust PCA decomposes the input data matrix X as

$$X = Z + S, \tag{14}$$

where Z is a low-rank matrix, and S is a sparse error matrix. The solution is obtained by solving

$$\begin{aligned} &\text{minimize} && ||Z||_* + \lambda_s ||S||_1 \\ &\text{subject to} && Z + S = X, \end{aligned} \tag{15}$$

where λ_s is a regularization weight.

However, straightforward application of the robust PCA algorithm is unsuitable for our data because our data have different characteristics in the matrix than what robust PCA algorithms address. Because of the rank-1 structure of irradiance matrices and the low-frequency nature of response functions, our data has one dominant singular value. This introduces confusion to robust PCA in determining the rank of our data, therefore it is difficult to set a proper λ_s for balancing these two costs. A larger λ_s favors more outliers remaining in the low-rank matrix Z, while a smaller λ_s prohibits rank variations, and even non-linear response functions can be treated as an outlier.

For these reasons, we make a simple modification to the original robust PCA for removing outliers. We iteratively decompose the matrix X into rank-1 and high-rank matrices, and apply thresholding to the high-rank matrix to find outliers according to the statistics of the high-rank matrix. The statistics are calculated with an assumption of the Gaussian distribution of rank deviations from the rank-1 approximation.

We show the outlier rejection process in Algorithm 1. In the algorithm table, R is a rank-1 matrix, N is a high-rank matrix, σ_i is the i^{th} singular value, u_i and v_i are i^{th} columns of U and V, respectively, and Ψ is a thresholding operator, defined as

Algorithm 1 Outlier Rejection Process

procedure OUTLIERREJECTION(X, ρ)
  $Z_0 = X$
  while not converged **do**
    $(U, \Sigma, V) = \text{svd}(Z_k)$
    $R = U\Sigma_1 V^T = \sigma_1 u_1 v_1^T$
    $N = Z_k - R$
    $dE = \Psi_\rho[N]$
    $Z_{k+1} = Z_k - dE$
  end while
  return Z^*
end procedure

$$\Psi_\rho[n_i] = \begin{cases} n_i & \text{if } |n_i - \mu_N| > \epsilon + \rho s_N \\ 0 & \text{otherwise,} \end{cases} \tag{16}$$

where ϵ is small epsilon value, and μ_N and s_N are the mean and standard deviation of N, respectively. The operator is extended to matrices by applying it to each element. Therefore, only outlier components out of ρ standard deviations remain in N.

3.3 Ambiguities

The estimated inverse response function $\hat{g}$ may suffer from ambiguities that are specific to the calibration setting. For example, a certain class of response functions f where $f(x)/f(ax) = \text{const.}$ holds cannot be handled in the varying illumination setting [4]. In the color mixture setting, we cannot determine response functions when both measured color distribution lies along the R=G=B line and RGB channel responses are identical [3]. In practice, these cases are rare while theoretically they exist.

One of the major ambiguities is *exponential ambiguity* in the multiple-exposure setting discussed by Grossberg and Nayar [10], *i.e.*, if g is a solution for $I = g(M)$, then g^γ can also become a solution as $I^\gamma = g^\gamma(M)$ for arbitrary γ. Recovery of the exposure ratios and the response function is impossible without either making assumptions on the response function or having rough estimates on the exposure ratios.

Without making any assumptions about exposure times, our method can robustly recover the response function up to the exponential ambiguity from at least two images. However, our method also suffers from this exponential ambiguity like other methods when the exposure times are completely unknown, because the rank-1 structure is retained even after any exponential function is applied. In short, if $\text{rank}(I) = 1$, then $\text{rank}(I^\gamma) = 1$ for any γ.

To resolve the ambiguity, we use only *one* known exposure ratio. Using the known exposure ratio, we can estimate γ by solving the least-square problem described

as

$$\hat{\gamma} = \underset{\gamma}{\operatorname{argmin}} \sum_{i,j} \left[\hat{g}^{\gamma}(M_i) - r_{i,j}\hat{g}^{\gamma}(M_j)\right]^2, \quad (17)$$

where $r_{i,j}$ is the exposure ratio e_i/e_j of measurement pairs M_i and M_j.

3.4 Representation of response functions

The empirical model of response function (EMoR) [7] and polynomial representation [2] are the most widely used representations of response functions. As mentioned in various prior works [3], [5], [16], [17], [18], [19], [23], EMoR can represent various response functions with few coefficients. However, it is difficult to compute derivatives for EMoR either analytically or numerically because EMoR is a highly non-smooth function. Therefore, EMoR is not suitable for gradient-based convex optimization. On the other hand, the polynomial representation is more appropriate for gradient-based convex optimization because of its smoothness. Also, recent research shows that most typical response functions can be represented well with only a 5^{th} order polynomial function [35]. For these reasons, we choose to use the polynomial representation as done in [2].

We normalize the irradiance and observation domains in the range of $[0, 1]$ by enforcing $g(0) = 0$ and $g(1) = 1$. We explicitly embed this boundary condition in the parametric representation of g, and the polynomial representation becomes

$$g(M) = M + M(M-1)\sum_{i=1}^{n-1} c_i M^{n-i-1}, \quad (18)$$

where n is the order of a polynomial function, and c_i are the coefficients to estimate. With this, the degree of freedom is reduced to only 4 for the 5-order polynomial representation.

3.5 Iterative optimization

We use the rank minimization and outlier rejection algorithms in an iterative manner to solve the problem. The overall process is summarized in Algorithm 2. Once the optimal solution of inverse response function g is obtained, if exponential ambiguity exists in the solution in the multiple-exposure setting, we resolve the exponential ambiguity γ after convergence using Eq. (17).

3.6 Prior model

In most cases, we can estimate a right solution from Eq. (13). However certain methods like color mixture case [3] have a difficulty to estimate a unique solution due to insufficient information. For that case, we can use prior information to regularize the solution. The prior model is formed by fitting a multivariate Gaussian mixture model to the DoRF database [7] as done in [3].

Algorithm 2 Radiometric Calibration Process

```
procedure RankCalib(D)
    initialize g
    while not converged do
        A = g ∘ D
        Z = OutlierRejection(A, ρ)
        Calculate error using Eq. (13)
        Update g
    end while
    return ĝ
end procedure
```

Using an Expectation Maximization (EM) algorithm, the prior model is constructed with K kernels as

$$p(g) = \sum_{i=1}^{K} \alpha_i \mathcal{N}(g; \mu_i, \Sigma_i). \quad (19)$$

The likelihood of the rank constraint is modeled as

$$p(D|g) = \frac{1}{Z}\exp\left(-\lambda E\left(g; D\right)\right), \quad (20)$$

where Z is a normalization constant, λ is a regularization parameter, and E is a rank error function. The optimal response function $\hat{g}$ is obtained by solving the following MAP problem:

$$\hat{g} = \underset{g}{\operatorname{argmax}}\, p\left(g; D\right) = \underset{g}{\operatorname{argmax}}\, p\left(D|g\right) p\left(g\right). \quad (21)$$

Substituting Eq. (19) and Eq. (20) into the logarithmic form of Eq. (21), we obtain

$$\hat{g} = \underset{g}{\operatorname{argmin}}\, \lambda E\left(g; D\right) - \log p(g). \quad (22)$$

The use of the prior information is demonstrated in Sec. 4.3.

4 Experiments

We evaluate the proposed method in three different settings: multiple-exposure, varying illumination, and color mixture settings. In particular, we make a thorough analysis of the proposed method using the multiple-exposure scenario in Sec. 4.1. Sec. 4.2 and Sec. 4.3 describe the result of varying illumination and color mixture cases, respectively.

The optimization of Eq. (13) can be performed using various minimizers. Though Eq. (13) is not convex, it converges to the correct solution with a broad range of input data as we will see below. In our experiments, we use the Levenberg-Marquardt (LM) method. We always set the weighting factor $\lambda = 1\text{e}10$ in Eq. (13) and $\rho = 3$ in Algorithm 1 throughout the experiments.

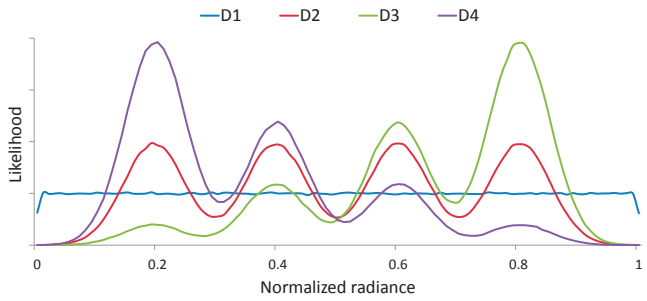

Fig. 3. Scene radiance distributions of four synthetic datasets (D1-D4).

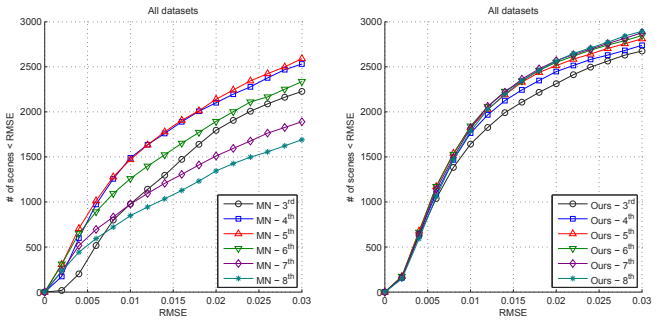

Fig. 4. Effect of numbers of coefficients of the polynomial representation.

4.1 Multiple-exposure case

To evaluate the proposed method, we perform experiments using both simulation and real-world data. We compare our results with results of Mitsunaga and Nayar's method [2] (MN method, henceforth). In our implementation, we use a polynomial function to represent response functions as described in Sec. 3.4 as done in [2]. Once the response function is estimated up to the exponential ambiguity, we resolve the ambiguity to determine the final response function using Eq. (17). This optimization is also performed using the LM method.

4.1.1 Simulation

In this section, we use a synthetic dataset for quantitative evaluation. The synthetic dataset is generated using the DoRF database [36], which contains 201 measured response functions. We synthetically generate scene radiances in the range of $[0, 1]$ and create 1000 observations (which forms a 1000-pixel image) using each response function with five exposure times. The step of exposure ratios is set to 0.5 because this is a commonly available setting in commercial cameras. Fig. 3 shows four scene radiance distributions (D1-D4) of the synthetic dataset that we have used. We further add five different magnitudes of noise for each radiance distribution. Therefore, the comparison with the MN method is performed using $4020 (= 201 \times 4 \times 5)$ synthetic data in total. Poisson noise distributions in Eq. (9) with camera gains $C_g (= \{0, 1, 3, 6, 9\})$ are used for diversifying the datasets.

In presenting the simulation result, we plot cumulative histograms that show the number of results below a certain root mean squared error (RMSE) for each configuration. The greater area under the curve shows the superior performance. On the top of each figure, we denote the radiance distribution used for the experiment. "All dataset" indicates that all the radiance distributions are used.

Initial guess. We first assess the effect of initial guesses to the solution. As mentioned, our method does not have a guarantee to converge to the globally optimal solution, like any other non-linear optimization problems. For this experiment, we use two settings; one is simply starting from a linear initial guess, and the other uses five different gamma curves as initial guesses of the inverse response function g and picks the optimal solution. In the latter setting, the range of γ is set to $0.8 - 1.6$ with a step of 0.2. In the experiment, we observe that our method as well as the MN method are not susceptible to the initial guess. The solution using our rank minimization approach may result in various local minima due to the exponential ambiguity. However, for radiometric calibration purposes, it is sufficient to find such a local minimum for our method because it is one of the true solutions with the exponential ambiguity in most cases. We use the linear response function as an initial guess for the rest of the evaluations for its simplicity.

Number of coefficients. One of the most important parameters for both methods is the number of coefficients in representing inverse response functions. In the polynomial representation, it is the degree of polynomial functions. To find the best number of coefficients, we perform performance evaluation with different numbers of coefficients, varying from 3$^{\text{rd}}$ to 8$^{\text{th}}$-order polynomials. Fig. 4 shows performance variations w.r.t. the polynomial orders for the MN method and our method. The MN method always produces a smaller cost value when higher-order polynomials are used. However, it does not necessarily mean a better estimation. Instead, it is due to an over-fitting problem, and it leads to worse estimates. We observed that for the MN method a 5$^{\text{th}}$ order polynomial works well with various noise levels. This result agrees with the observation in [35], where it is said that a 5$^{\text{th}}$ order polynomial representation has a good balance between accuracy and flexibility in representing response functions.

On the other hand, normally our method shows better results as the polynomial order increases. In our method, the smaller cost values coincide well with the precision of estimates. We decide to use a 6$^{\text{th}}$ order polynomial for our method because we observe that there is no performance gain from a polynomial order higher than the 6$^{\text{th}}$ order.

Condition numbers and image noise. In Sec. 3, we

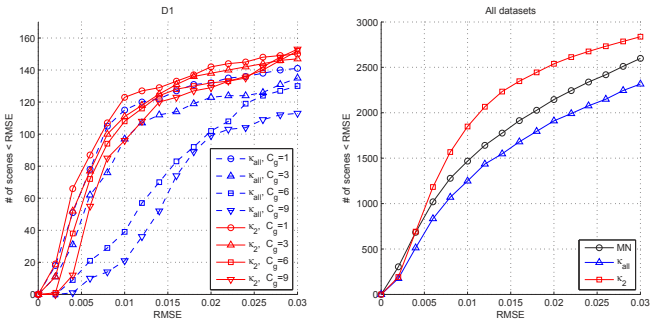

Fig. 5. (Left) Evaluation of cost functions of Eq. (8) and Eq. (12) using synthetic scenes D1. "κ_{all}" indicates minimization of all the condition numbers using Eq. (8), while "κ_2" corresponds to minimization of 2nd condition number using Eq. (12). (Right) Performance comparison of the MN method, Eq. (8) and Eq. (12)

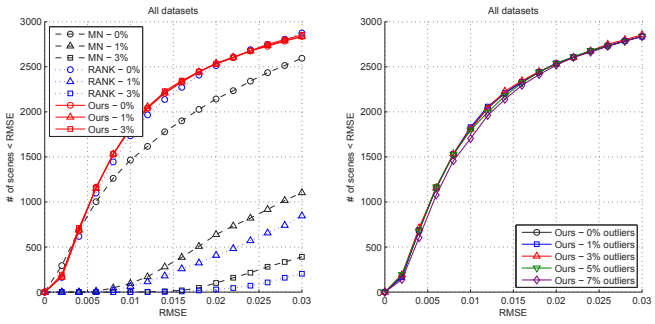

Fig. 6. (Left) Effect of outliers on different methods. MN indicates the MN method, RANK is a straightforward rank minimization without outlier rejection, and Ours is our complete method. (Right) Performance comparison of our method with different amounts of outliers.

observed the relation between condition numbers and image noise. Here, we perform experiments for further validation. For this experiment, we compare the results of two cost functions, Eq. (8) and Eq. (12). Eq. (8) minimizes the sum of all condition numbers, while Eq. (12) minimizes only the 2nd condition number. The experimental results are shown in Fig. 5. In the left plot, it shows that minimizing the 2nd condition number is much more robust than minimizing the sum of all condition numbers, especially when there is greater noise. The right figure shows the cumulative histogram of the MN method, Eq. (8) and Eq. (12) for all of datasets. In this figure, the result of Eq. (8) shows worse result than the result of the MN method, while Eq. (12) shows the best result among the others.

Outliers. In practice, recorded data have outliers due to misalignment of images or small motion in a scene. To validate our outlier rejection procedure, we perform experiments by adding outliers in the dataset. The outliers are added by randomly changing selected pixel values in the range of $[0, 1]$ of the original dataset. Fig. 6 shows results. While our method with outlier rejection procedure is not affected by outliers, performances of other methods, *i.e.*, straightforward rank minimization and the MN method, are highly degraded even for only one percent outliers.

Results with synthetic dataset. Now we assess the performance of our method in comparison with the MN method. Fig. 7 shows results with the synthetic dataset. With very small noise, the MN method works better than ours. However, the performance of the MN method rapidly degrades as the noise becomes larger while our method is still robust against the greater noise level. As shown in the figure, the estimation accuracy depends on not only the noise level but also the radiance distribution. With uniformly distributed scene radiance, the estimation becomes quite stable for both methods. However, when the radiance distribution becomes biased, which is very common, it introduces performance degradation particularly for the MN method as shown in the D4 result. The biased radiance distribution introduces biased observations, thus it yields an over-fitting problem in the MN method. In contrast, our method suffers less from such an effect.

We summarize the quantitative results in Table 2. The DoRF database contains some response functions which are difficult to represent with 5th order polynomials. These functions give trivial results for the MN method; therefore, we only use the best 150 fitting results for each of the algorithms to compute the mean and standard deviation of RMSE and disparity (the maximum deviation from the ground truth). The table shows that our method performs well for most datasets. It also shows that our method is robust against increasing noise levels, while the performance of the MN method rapidly degrades.

4.1.2 *Real-world experiment*

We also perform experiments using real-world cameras and scenes. In our experiments, we use three different cameras: Canon 550D, Nikon D1X, and Sony DSC-828. Each dataset is collected by capturing a static scene with different exposure times. Fig. 8 shows estimation results with real-world scenes. For presenting the results, we convert images to irradiances as done in [37] and compare the results both with and without calibration. We estimate response functions from a set of input images and linearize the input by applying estimated inverse response functions. For the estimation of response functions, we first reject observations in the under-exposure level (*e.g.*, 5 in 0-255 range) and saturation level (*e.g.*, 250 in 0-255 range) to avoid estimation bias. There are white balancing and color space transformation to convert camera color space into the linear sRGB. The transformation that includes both the white balancing and the color space transformation can be represented by a 3×3 matrix and can be obtained in the least-square manner. The error maps are calculated by comparing the estimated

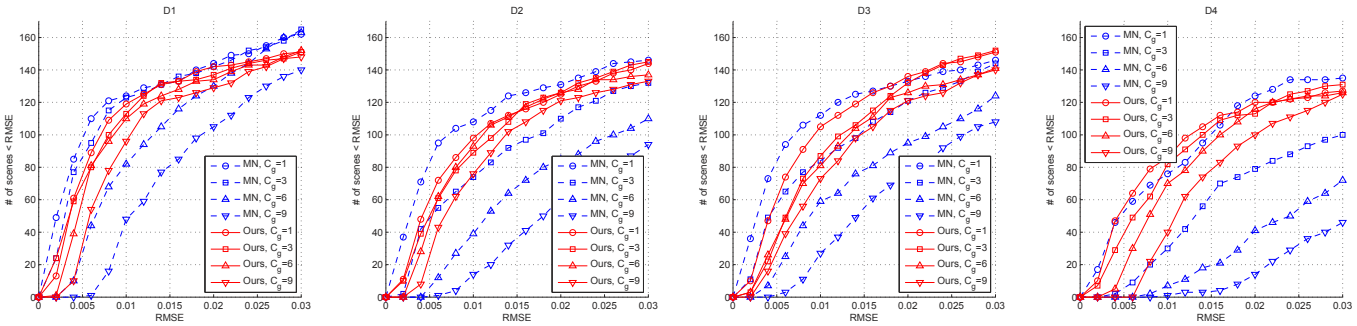

Fig. 7. Cumulative histogram of the number of successful cases w.r.t. RMSE.

			Mean					Standard Deviation				
Noise level (C_g)			0	1	3	6	9	0	1	3	6	9
D1	RMSE	MN	**0.0058**	**0.0054**	**0.0062**	0.0109	0.0160	**0.0054**	**0.0057**	**0.0056**	**0.0063**	0.0075
		Ours	0.0071	0.0070	0.0075	**0.0084**	**0.0102**	0.0054	0.0060	0.0067	0.0067	**0.0070**
	Disparity	MN	**0.0142**	**0.0139**	**0.0152**	0.0238	0.0354	0.0134	**0.0140**	**0.0139**	**0.0147**	0.0194
		Ours	0.0157	0.0164	0.0174	**0.0194**	**0.0225**	**0.0124**	0.0143	0.0153	0.0164	**0.0179**
D2	RMSE	MN	**0.0079**	**0.0077**	0.0134	0.0208	0.0287	**0.0076**	**0.0081**	0.0107	0.0133	0.0174
		Ours	0.0095	0.0100	**0.0105**	**0.0111**	**0.0132**	0.0082	0.0086	**0.0083**	**0.0094**	**0.0098**
	Disparity	MN	**0.0180**	**0.0184**	0.0299	0.0468	0.0634	0.0172	0.0190	0.0239	0.0304	0.0370
		Ours	0.0196	0.0214	**0.0228**	**0.0240**	**0.0285**	**0.0163**	**0.0183**	**0.0186**	**0.0207**	**0.0227**
D3	RMSE	MN	**0.0076**	**0.0074**	0.0111	0.0174	0.0234	0.0072	0.0080	0.0092	0.0117	0.0141
		Ours	0.0080	0.0086	**0.0105**	**0.0116**	**0.0128**	**0.0066**	**0.0069**	**0.0068**	**0.0086**	**0.0085**
	Disparity	MN	**0.0170**	**0.0176**	0.0250	0.0398	0.0521	0.0164	0.0180	0.0207	0.0282	0.0309
		Ours	0.0173	0.0184	**0.0218**	**0.0245**	**0.0272**	**0.0142**	**0.0139**	**0.0137**	**0.0182**	**0.0193**
D4	RMSE	MN	**0.0086**	**0.0118**	0.0233	0.0393	0.0565	**0.0079**	**0.0097**	0.0152	0.0252	0.0344
		Ours	0.0144	0.0131	**0.0138**	**0.0154**	**0.0189**	0.0138	0.0134	**0.0124**	**0.0118**	**0.0126**
	Disparity	MN	**0.0195**	**0.0262**	0.0507	0.0822	0.1155	**0.0184**	**0.0221**	0.0331	0.0486	0.0635
		Ours	0.0285	0.0275	**0.0293**	**0.0327**	**0.0393**	0.0270	0.0276	**0.0273**	**0.0275**	**0.0308**

TABLE 2
Quantitative results using the synthetic dataset in comparison with Mitsunaga and Nayar's method (MN) in terms of the RMSE and disparity over various datasets.

RAW images with the ground truth RAW images. The error in the estimated RAW images with calibration is due to a gamut mapping [37] at saturated pixels and demosaicing/compression around edges. For comparison, we also estimate the response function using the MN method from the same input data. With reasonable input, both methods present similar estimation results.

To evaluate the performance using diverse response functions, we additionally perform an experiment with a Point Grey Flea3 camera. With the camera, we can choose any gamma function as a response function. Three different gamma functions ($\gamma = \{0.6, 1.0, 2.2\}$) are used, and the result is shown in Fig. 9. For various types of gamma functions, our method performs well while the MN method fails to estimate the right solution for $\gamma = 0.6$.

Radiometric alignment. To perform radiometric alignment without any exposure information, all we need is a simple constraint to anchor the solution. In our case, we derive a response function, which satisfies that the observation 0.5 is mapped to an irradiance 0.5. Note that the constraint is arbitrary for the radiometric alignment application as long as a unique radiometric response function, which may differ from the true response function by the exponential ambiguity, is determined. Based on this, we estimate the (pseudo) exposure ratios of input images and perform the radiometric alignment.

Here we show a radiometric alignment result using the estimated response function in Fig. 10. Without calibration, the aligned image with proper intensity normalization using the ratio of (R+G+B) intensity gives an RMSE of 0.0657. After calibration with our method, the error is reduced to 0.0225.

4.2 Varying illumination case

We apply our method to the varying illumination case and compare with the method proposed by Shi *et al.* [4]. We use two real-world scenes SHEEP and FROG recorded by a Canon 20D and Nikon D70, respectively. The ground truth is obtained by the MN method using a Macbeth Color Chart beforehand.

For each scene, we randomly select samples to produce color profiles and compute the average of the results of ten trials. In practice, the accuracy of Shi *et al.*'s method has dependency on the selected samples, therefore we take more trials and remove obvious failure

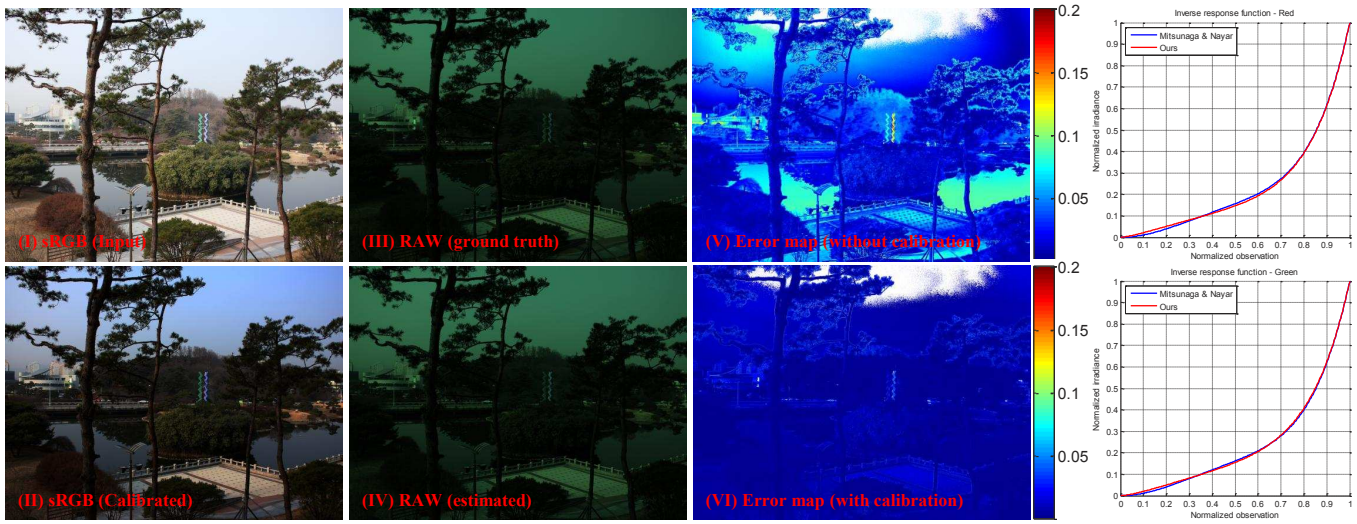

(a) Canon 550D

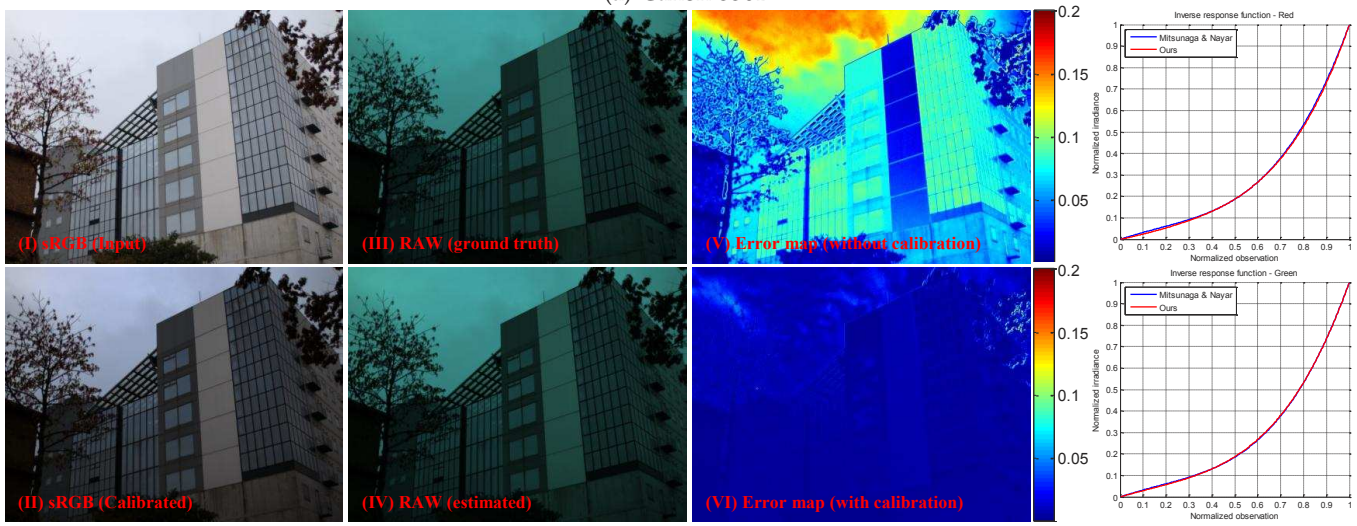

(b) Nikon D1X

(c) Sony DSC-F828

Fig. 8. Results of our calibration method. From top to bottom, the results of different cameras are shown: (a) Canon 500D, (b) Nikon D1X, and (c) Sony DSC-F828. For each camera, several images are shown: (I) one of the input images, (II) the calibrated image by applying estimated inverse response functions, (III) the ground truth RAW image, (IV) the estimated RAW image from the calibrated sRGB image, (V) error map between the ground truth RAW image and the estimated RAW image without calibration, (VI) error map between the ground truth RAW image and the estimated RAW image with calibration. The white pixels on the error maps indicate saturated pixels having a value of 255 in any of the channels. The right column shows estimated inverse response functions.

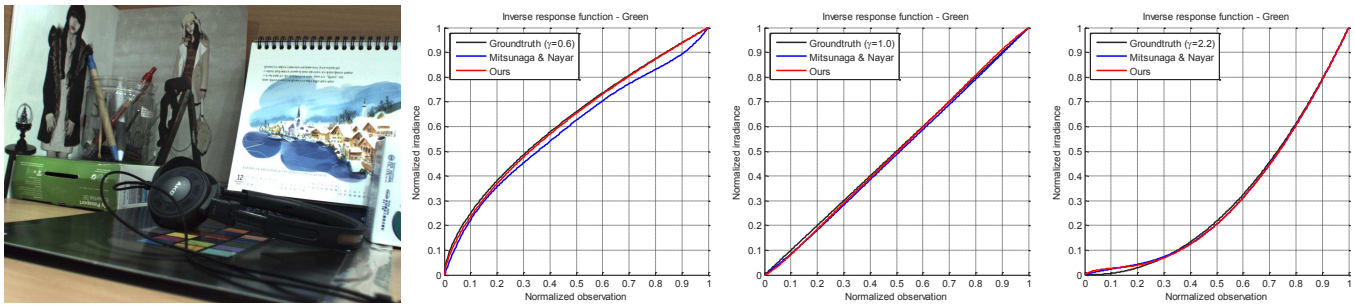

Fig. 9. Results of our calibration method with a dataset captured from a Point Grey Flea3 camera.

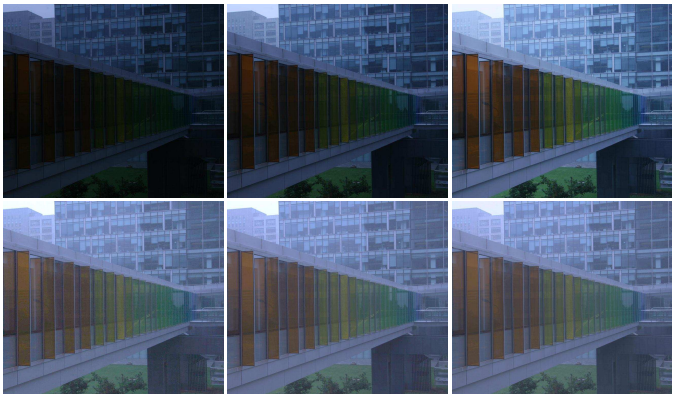

Fig. 10. Radiometric alignment of real-world images. Top: input images, Bottom: radiometrically aligned images.

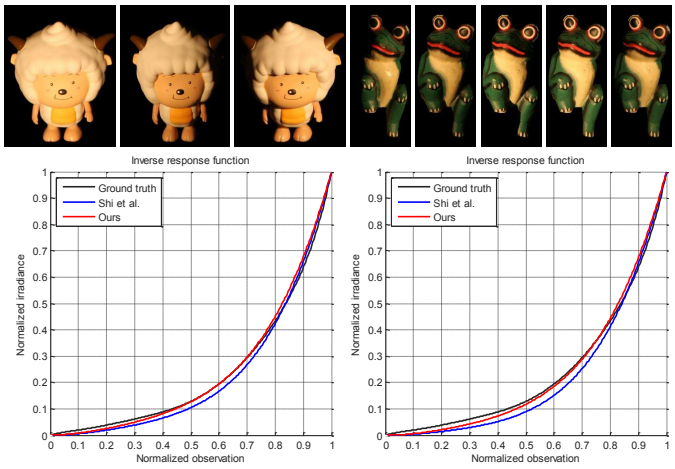

SHEEP (12) FROG (20)

Fig. 11. (Top) example images of SHEEP and FROG dataset. (Bottom) result of radiometric calibration in the varying illumination case. SHEEP dataset is recorded by a Canon 20D (12 images) and FROG data is recorded by a Nikon D70 (20 images).

modes. In this experiment, for the purpose of directly comparing our rank constraint with Shi *et al.*'s non-linearity constraint, we do not apply the outlier rejection process.

Fig. 11 shows the results. In the figure, the median response curve of ten trials is used for plotting. We also summarize the quantitative results in Table 3. For both datasets, our method shows more accurate and stable results. With a small number of samples, the result of the original method fluctuates because of the heuristic non-linearity constraint, but our method robustly converges well because of the more principled computation scheme. With more samples, both methods give more stable and robust estimation. As shown in the table, our method is about 1000 times faster than the original method that uses Nelder-Mead simplex optimization [38]. Since our method has a computational complexity of $O(n)$, we can use more samples to achieve far more robust estimation.

4.3 Color mixture case

We also perform radiometric calibration from a single image, which utilizes the linearity of color mixtures around texture edges [3]. This method relies on prior information of response functions because color mixtures usually only span a limited range of observations, which is not sufficient to uniquely determine the response function. Therefore, Lin *et al.* [3] infer the solution using a Bayesian approach with prior information of real-world camera response functions [7]. In [3], the linearity of color mixtures is measured using the distance from each mixed color to the line defined by the two colors in the RGB color space.

We also use prior information to regularize the solution as explained in Sec. 3.6. There is a trade-off in using the prior information between estimation bias and robustness. Therefore, a strong prior might introduce bias in the estimation result. In our implementation, we use five kernels ($K = 5$) to construct the prior model and λ is set empirically to 10^3. The rank error function E is defined as

$$E(g; D) = \sum_{i=1}^{m} w_i \kappa_2 (A_i) \quad \text{s.t.} \quad A_i = g \circ D_i, \tag{23}$$

where m is the number of color mixtures, and w_i is a

Dataset		SHEEP (Canon 20D)			FROG (Nikon D70)		
samples	method	RMSE (std.)	Disparity (std.)	Time(s)	RMSE (std.)	Disparity (std.)	Time(s)
50	Shi *et al.* [4]	0.0488 (0.0227)	0.0846 (0.0429)	433.66	0.0279 (0.0050)	0.0456 (0.0064)	697.05
	Ours	**0.0226 (0.0006)**	**0.0447 (0.0061)**	**0.84**	**0.0191 (0.0010)**	**0.0419 (0.0051)**	**0.80**
100	Shi *et al.* [4]	0.0418 (0.0172)	0.0729 (0.0345)	914.64	0.0293 (0.0038)	0.0441 (0.0056)	1316.88
	Ours	**0.0218 (0.0003)**	**0.0430 (0.0021)**	**1.11**	**0.0176 (0.0005)**	**0.0396 (0.0032)**	**0.86**

TABLE 3
Radiometric calibration results in the varying illumination case. SHEEP/FROG dataset captured by Canon 20D and Nikon D70 are used. The average RMSE of ten trials are shown. The value inside the brackets is the standard deviation of the ten trials.

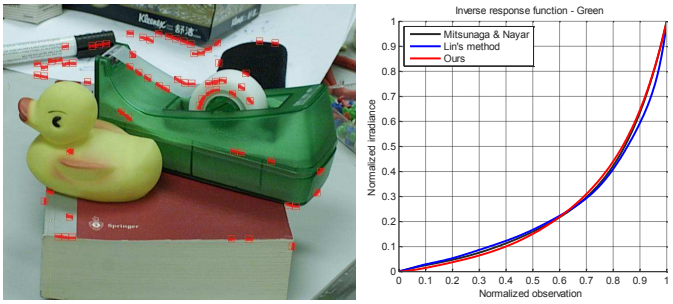

Fig. 12. Radiometric calibration from a single image. Lin *et al*.'s result is obtained from their original paper. Data courtesy of Stephen Lin.

weighting parameter. The parameter w_i is defined as the distance between the two irradiances of a color mixture in the RGB space because a color mixture that has longer distance is affected more by response functions. The coefficients of g is initially set to the mean inverse response function of the DoRF database [7].

Fig. 12 shows the result for the input image used in [3]. The estimation result is compared with the ground truth that is obtained by MN method beforehand. While this case requires prior information, the result shows that low-rank constraint can be applied well in color mixture based methods.

5 CONCLUSIONS

In this paper, we have introduced a robust radiometric calibration algorithm that uses the low-rank structure of irradiance vectors. The problem is formulated as one of rank minimization and solved by minimization of the condition number of the input matrix. We further developed an algorithm for outlier rejection. These methods are combined in an iterative manner for achieving robust estimation. The advantage of our method is that it capitalizes on the fundamental linear dependency of sensor irradiances, therefore it can handle the radiometric calibration problem in a unified and principled framework. We show that our framework can be easily applied to other radiometric calibration problems that use linearity of irradiance by taking Shi *et al.*'s [4] and Lin *et al.*'s [3] methods as examples. The effectiveness of the proposed approach is verified using both simulation and real-world experiments.

5.1 Limitations

In our current implementation, we use a simple optimizer for the rank minimization, and it is sufficient to find the right solution as shown in experiments for most of the cases. However, sometimes the optimization fails to converge to the global minimum, or converges to a trivial solution due to insufficient input data or great noise. This could be improved by using a better optimization method for the rank minimization.

ACKNOWLEDGMENTS

Joon-Young Lee is partially supported by National Strategic R&D Program for Industrial Technology, Korea, and by the National Research Foundation of Korea(NRF) grant funded by the Korea government(MEST) (No.2011-0018250). The research described in this document, conducted by Kausushi Ikeuchi, is supported in part by the Global Research Network program (No. D00096(I00363)) of National Research Foundation of Korea.

REFERENCES

[1] P. Debevec and J. Malik, "Recovering high dynamic range radiance maps from photographs," in *Proceedings of ACM SIGGRAPH*, 1997, pp. 369–378. 1, 2

[2] T. Mitsunaga and S. K. Nayar, "Radiometric self calibration," in *Proceedings of IEEE Conference on Computer Vision and Pattern Recognition (CVPR)*, 1999, pp. 374–380. 1, 2, 4, 7, 8

[3] S. Lin, J. Gu, S. Yamazaki, and H.-Y. Shum, "Radiometric calibration from a single image," in *Proceedings of IEEE Conference on Computer Vision and Pattern Recognition (CVPR)*, 2004, pp. 938–945. 1, 3, 4, 6, 7, 12, 13

[4] B. Shi, Y. Matsushita, Y. Wei, C. Xu, and P. Tan, "Self-calibrating photometric stereo," in *Proceedings of IEEE Conference on Computer Vision and Pattern Recognition (CVPR)*, 2010, pp. 1118–1125. 1, 3, 4, 6, 10, 13

[5] S. J. Kim and M. Pollefeys, "Robust radiometric calibration and vignetting correction," *IEEE Transactions on Pattern Analysis and Machine Intelligence*, vol. 30, no. 4, pp. 562–576, 2008. 1, 2, 7

[6] S. Mann and R. Picard, "On being 'undigital' with digital cameras: extending dynamic range by combining differently exposed pictures," in *Proceedings of IS & T, 48th annual conference*, 1995, pp. 422–428. 2

[7] M. Grossberg and S. K. Nayar, "Modeling the space of camera response functions," *IEEE Transactions on Pattern Analysis and Machine Intelligence*, vol. 26, no. 10, pp. 1272–1282, 2004. 2, 7, 12, 13

[8] S. K. Nayar and T. Mitsunaga, "High dynamic range imaging: spatially varying pixel exposures," in *Proceedings of IEEE Conference on Computer Vision and Pattern Recognition (CVPR)*, 2000, pp. 472–479. 2

[9] S. Mann and R. Mann, "Quantigraphic imaging: Estimating the camera response and exposures from differently exposed images," in *Proceedings of IEEE Conference on Computer Vision and Pattern Recognition (CVPR)*, 2001, pp. 842–849. 2

[10] M. Grossberg and S. K. Nayar, "Determining the camera response from images: what is knowable?" *IEEE Transactions on Pattern Analysis and Machine Intelligence*, vol. 25, no. 11, pp. 1455–1467, 2003. 2, 6

[11] A. Litvinov and Y. Y. Schechner, "Addressing radiometric nonidealities: a unified framework," in *Proceedings of IEEE Conference on Computer Vision and Pattern Recognition (CVPR)*, 2005, pp. 52–59. 2

[12] H. Farid, "Blind inverse gamma correction," *IEEE Transactions on Image Processing*, vol. 10, no. 10, pp. 1428–1433, 2001. 2

[13] Y. Tsin, V. Ramesh, and T. Kanade, "Statistical calibration of CCD imaging process," in *Proceedings of International Conference on Computer Vision (ICCV)*, 2001, pp. 480–487. 3

[14] C. Pal, R. Szeliski, M. Uyttendale, and N. Jojic, "Probability models for high dynamic range imaging," in *Proceedings of IEEE Conference on Computer Vision and Pattern Recognition (CVPR)*, 2004, pp. 173–180. 3

[15] T.-T. Ng, S.-F. Chang, and M.-P. Tsui, "Using geometry invariants for camera response function estimation," in *Proceedings of IEEE Conference on Computer Vision and Pattern Recognition (CVPR)*, 2007, pp. 1–8. 3

[16] Y. Matsushita and S. Lin, "Radiometric calibration from noise distributions," in *Proceedings of IEEE Conference on Computer Vision and Pattern Recognition (CVPR)*, 2007, pp. 1–8. 3, 7

[17] J. Takamatsu, Y. Matsushita, and K. Ikeuchi, "Estimating camera response functions using probabilistic intensity similarity," in *Proceedings of IEEE Conference on Computer Vision and Pattern Recognition (CVPR)*, 2008, pp. 1–8. 3, 7

[18] ——, "Estimating radiometric response functions from image noise variance," in *Proceedings of European Conference on Computer Vision (ECCV)*, 2008, pp. 623–637. 3, 7

[19] S. Lin and L. Zhang, "Determining the radiometric response function from a single grayscale image," in *Proceedings of IEEE Conference on Computer Vision and Pattern Recognition (CVPR)*, 2005, pp. 66–73. 3, 7

[20] B. Wilburn, H. Xu, and Y. Matsushita, "Radiometric calibration using temporal irradiance mixtures," in *Proceedings of IEEE Conference on Computer Vision and Pattern Recognition (CVPR)*, 2008, pp. 1–7. 3, 4

[21] C. Manders, C. Aimone, and S. Mann, "Camera response function recovery from different illuminations of identical subject matter," in *Proceedings of International Conference on Image Processing (ICIP)*, 2004, pp. 2965–2968. 3

[22] K. Shafique and M. Shah, "Estimation of the radiometric response functions of a color camera from differently illuminated images," in *Proceedings of International Conference on Image Processing (ICIP)*, 2004, pp. 2339–2342. 3

[23] S. J. Kim, J.-M. Frahm, and M. Pollefeys, "Radiometric calibration with illumination change for outdoor scene analysis," in *Proceedings of IEEE Conference on Computer Vision and Pattern Recognition (CVPR)*, 2008, pp. 1–8. 3, 7

[24] M. Turk and A. Pentland, "Eigenfaces for recognition," *Journal of Cognitive Neuroscience*, vol. 3, no. 1, pp. 71–86, 1991. 3

[25] C. Tomasi and T. Kanade, "Shape and motion from image streams under orthography: a factorization method," *International Journal on Computer Vision*, vol. 9, no. 2, pp. 137–154, 1992. 3

[26] H. Hayakawa, "Photometric stereo under a light source with arbitrary motion," *Journal of the Optical Society of America*, vol. 11, no. 11, pp. 3079–3089, 1994. 3

[27] Y. Peng, A. Ganesh, J. Wright, W. Xu, and Y. Ma, "RASL: Robust alignment by sparse and low-rank decomposition for linearly correlated images," in *Proceedings of IEEE Conference on Computer Vision and Pattern Recognition (CVPR)*, 2010, pp. 763–770. 3, 5

[28] M. Paladini, A. Bartoli, and L. Agapito, "Sequential non-rigid structure-from-motion with the 3D-implicit low-rank shape model," in *Proceedings of European Conference on Computer Vision (ECCV)*, 2010, pp. 15–28. 3

[29] Z. Zhang, A. Ganesh, X. Liang, and Y. Ma, "Tilt: Transform invariant low-rank textures," in *Proceedings of Asian Conference on Computer Vision (ACCV)*, 2010, pp. 314–328. 3, 5

[30] L. Wu, A. Ganesh, B. Shi, Y. Matsushita, Y. Wang, and Y. Ma, "Robust photometric stereo via low-rank matrix completion and recovery," in *Proceedings of Asian Conference on Computer Vision (ACCV)*, 2010, pp. 703–717. 3, 5

[31] Z. Zhang, Y. Matsushita, and Y. Ma, "Camera calibration with lens distortion from low-rank textures," in *Proceedings of IEEE Conference on Computer Vision and Pattern Recognition (CVPR)*, 2011, pp. 2321–2328. 3

[32] J.-Y. Lee, B. Shi, Y. Matsushita, I.-S. Kweon, and K. Ikeuchi, "Radiometric calibration by transform invariant low-rank structure," in *Proceedings of IEEE Conference on Computer Vision and Pattern Recognition (CVPR)*, 2011, pp. 2337–2344. 3

[33] J. Wright, A. Ganesh, S. Rao, Y. Peng, and Y. Ma, "Robust principal component analysis: Exact recovery of corrupted low-rank matrices by convex optimization," in *Proceedings of Neural Information Processing Systems*, 2009. 4, 5, 6

[34] Y. Hwang, J.-S. Kim, and I. S. Kweon, "Difference-based image noise modeling using skellam distribution," *IEEE Transactions on Pattern Analysis and Machine Intelligence*, 2011. 5

[35] A. Chakrabarti, D. Scharstein, and T. Zickler, "An empirical camera model for internet color vision," in *Proceedings of British Machine Vision Conference (BMVC)*, 2009. 7, 8

[36] M. Grossberg and S. K. Nayar, "What is the space of camera response functions?" in *Proceedings of IEEE Conference on Computer Vision and Pattern Recognition (CVPR)*, 2003, pp. 602–609. 8

[37] H. T. Lin, S. J. Kim, S. Susstrunk, and M. S. Brown, "Revisiting radiometric calibration for color computer vision," *Proceedings of International Conference on Computer Vision (ICCV)*, 2011. 9, 10

[38] J. Nelder and R. Mead, "A simplex method for function minimization," *Computer Journal*, vol. 7, pp. 308–313, 1965. 12